

## Article

# Effects of Annealing on Hydrogen Storage Performance in TiZrCrMnFeNi High-Entropy Alloy

Tengfei Cheng <sup>1,\*</sup>, Jing Huang <sup>1</sup>, Wanggang Fang <sup>1</sup>, Liqing He <sup>1,\*</sup>, Xiangqun Duan <sup>1</sup>, Guotong Zou <sup>2</sup>, Xiao Li <sup>1</sup> and Xinghai Ren <sup>1</sup>

<sup>1</sup> Hefei General Machinery Research Institute Co., Ltd., Hefei 230031, China

<sup>2</sup> School of Materials Science and Engineering, Central South University, Changsha 410083, China

\* Correspondence: tfchengshu@163.com (T.C.); heli\_limao@163.com (L.H.)

**Abstract:** This study employed annealing heat treatment ranging from 900 to 1300 °C to systematically investigate the effects of annealing temperature on the microstructure and hydrogen storage performance of the equimolar TiZrCrMnFeNi high-entropy alloy. The research indicates that the TiZrCrMnFeNi high-entropy alloy is composed of the C14 Laves phase and a small amount of cubic phase. Compared to the as-cast alloy, the alloy annealed at high temperature (1000~1200 °C) exhibited increased microstructure homogeneity, a higher content of the C14 Laves phase, and a significant enhancement in hydrogen storage capacity. The annealing heat treatment led to changes in the unit cell volume of the C14 Laves phase, with an inverse relationship between unit cell volume and hydrogen absorption and desorption plateau pressures. An increase in unit cell volume resulted in a lower desorption plateau pressure, making the desorption reaction more difficult and consequently increasing the enthalpy change for desorption. This study not only reveals the intrinsic relationship between annealing temperature and the hydrogen storage performance of high-entropy alloys, but also provides significant experimental evidence and theoretical guidance for the design and development of high-entropy alloy materials with excellent hydrogen storage characteristics.



Academic Editor: Heinz-Günter Brokmeier

Received: 28 February 2025

Revised: 14 March 2025

Accepted: 22 March 2025

Published: 25 March 2025

**Citation:** Cheng, T.; Huang, J.; Fang, W.; He, L.; Duan, X.; Zou, G.; Li, X.; Ren, X. Effects of Annealing on Hydrogen Storage Performance in TiZrCrMnFeNi High-Entropy Alloy. *Crystals* **2025**, *15*, 297. <https://doi.org/10.3390/crust15040297>

**Copyright:** © 2025 by the authors. Licensee MDPI, Basel, Switzerland. This article is an open access article distributed under the terms and conditions of the Creative Commons Attribution (CC BY) license (<https://creativecommons.org/licenses/by/4.0/>).

## 1. Introduction

The global energy transition and prominent environmental issues have highlighted the importance of hydrogen energy as a clean secondary energy source, which is crucial for achieving the goals of carbon peak and carbon neutrality, attracting widespread attention from various countries [1–5]. The key to the large-scale application of hydrogen energy lies in safe and efficient storage and transport technologies, with hydrogen storage being a bottleneck in the development of the hydrogen energy industry. Solid-state hydrogen storage has become a research hotspot due to its high energy density and safety, among which metal hydrides are promising hydrogen storage technologies because of their high volumetric hydrogen storage density and the absence of stringent conditions [6–8]. High-entropy alloy (HEA), first proposed by Yeh [9] and Cantor [10] in 2004, is an emerging material with superior performance and has become a new field in materials science [11,12]. Its multi-component alloy design strategy is beneficial for improving hydrogen storage capacity and hydrogen absorption/desorption performance, making it a hot topic in the development of high-capacity hydrogen storage alloys [13–15].

In particular, the equimolar TiZrCrMnFeNi HEA developed by Parisa Edalati [16] has shown reversible hydrogen storage and ultra-fast hydrogen absorption kinetics at room temperature. The performance of TiZrCrMnFeNi HEA is compared with other known and widely used hydrogen storage materials, as shown in Table 1. The reversible mass hydrogen storage density of TiZrCrMnFeNi HEA is relatively low. However, its hydrogen absorption kinetics and cyclic stability are superior, indicating that its overall hydrogen storage performance is excellent.

Its hydrogen storage performance, however, still needs further improvement. Annealing is a traditional material modification technique that can adjust the microstructure and crystal defects to improve macroscopic properties. Appropriate heat treatment can significantly affect the microstructure of alloys and optimize their hydrogen storage performance [17–19]. This study, based on the phase diagram of the TiZrCrMnFeNi HEA [16], explores the optimization of hydrogen storage performance through high-temperature annealing heat treatment. The effects of different annealing temperatures on the hydrogen storage properties of the alloy were systematically studied, and the relationship between the annealing temperature and the hydrogen storage properties of the alloy was revealed. Furthermore, this study elucidates the mechanism by which annealing temperature regulates the hydrogen storage performance of HEA, providing significant experimental evidence and theoretical guidance for the development of HEA materials with excellent hydrogen storage characteristics.

**Table 1.** Comparison of the comprehensive hydrogen storage performance of different hydrogen storage alloy systems.

Hydrogen Storage Alloy	Reversible Mass Hydrogen Storage Density (wt.%)	Hydrogen Absorption/Desorption Temperature (°C)	Initial Hydrogen Absorption Kinetics	Cyclic Stability	Ref.
LaNi <sub>5</sub>	1.2–1.4	Room temperature	Excellent	Excellent	[20,21]
TiFe TiMn	1.6–1.8	Room temperature	Poor	Good	[22]
V-Ti-Cr					
V-Ti-Mn	2.0–2.4	Room temperature	Moderately Poor	Poor	[23,24]
V-Ti-Fe					
Mg <sub>2</sub> Si	3.6–7.6	≥300	Moderately Poor	Good	[25,26]
Mg <sub>2</sub> Fe					
TiZrCrMnFeNi	1.6–1.7	Room temperature	Excellent	Excellent	[16]

## 2. Materials and Methods

### 2.1. Material Preparation

The hydrogen storage alloy was prepared using a vacuum arc furnace (WK-II). The melting process was repeated six times to ensure a relatively uniform alloy structure. After melting, the surfaces of the hydrogen storage alloy were successively ground with sandpaper to remove the surface oxide layer and impurities. The alloy was then placed into a high-temperature tube furnace (RHTC 80/450/15). The heating rate was set at 200 °C/h, and the furnace was heated to temperatures ranging from 900 to 1300 °C, with a holding time of 2 h for each temperature. Throughout the entire heating and holding process, argon gas was continuously flowing at a rate of 200 L/h. After the holding period, the cooling rate of the alloy during annealing was controlled at 10–50 °C/h.

### 2.2. Microstructural Characterization

The alloy block is ground using a tungsten carbide mortar and then sieved to obtain alloy powder with a particle size of 100–200 mesh. The alloy powder was subjected to X-ray diffraction analysis (XRD) using a Rigaku Dmax 2500 V instrument. The Cu target

$\text{K}\alpha$  ray was selected for testing, and the scanning range was  $30\text{--}90^\circ$ . The Rietveld method was combined with XRD to analyze the phase composition of the high-entropy alloy and the structural evolution during hydrogen absorption/desorption. Scanning electron microscopy (SEM, Apreo S HiVac, is manufactured by Thermo Fisher Scientific, which is headquartered in Waltham, MA, USA) and energy-dispersive spectroscopy (EDS) were employed to closely examine the morphological and microstructural changes in the alloy before and after hydrogen absorption/desorption, along with the elemental distribution within the alloy system.

### 2.3. Absorption/Desorption Tests

All alloy ingots were manually crushed, sieved, and 100–200 mesh samples were taken for testing. A high-pressure hydrogen storage adsorption instrument (Caspro) was used to determine the kinetics of the hydrogen absorption/desorption process and the PCT (pressure–composition–temperature) curves of the alloy powder. This allowed for the acquisition of equilibrium hydrogen pressures, reversible capacities, and thermodynamic parameters at different temperatures. Additionally, volumetric methods were employed to measure the isothermal hydrogen absorption/desorption kinetics of the alloy.

## 3. Results and Discussions

### 3.1. Microstructure and Phase Composition

Figure 1 presents the X-ray diffraction (XRD) phase analysis of the TiZrCrMnFeNi high-entropy alloy under various conditions, including as-cast and several annealed states. Specifically, Figure 1 clearly reveals that the alloy is primarily composed of the C14 Laves phase, along with a minor cubic phase. The sharp and well-defined peaks observed in the XRD pattern are indicative of the high crystallinity and excellent crystal structure of the alloy samples. This perfect crystallinity suggests that the alloy has undergone minimal defects or dislocations during its formation process. Notably, there are distinct variations in the intensity of the diffraction peaks corresponding to the C14 Laves phase across different samples. These variations are significant as they provide insights into the changes in the microstructure and elemental distribution within the alloy. For instance, differences in peak intensity may arise from variations in the concentration or distribution of alloying elements, which can influence the overall stability and properties of the C14 Laves phase.

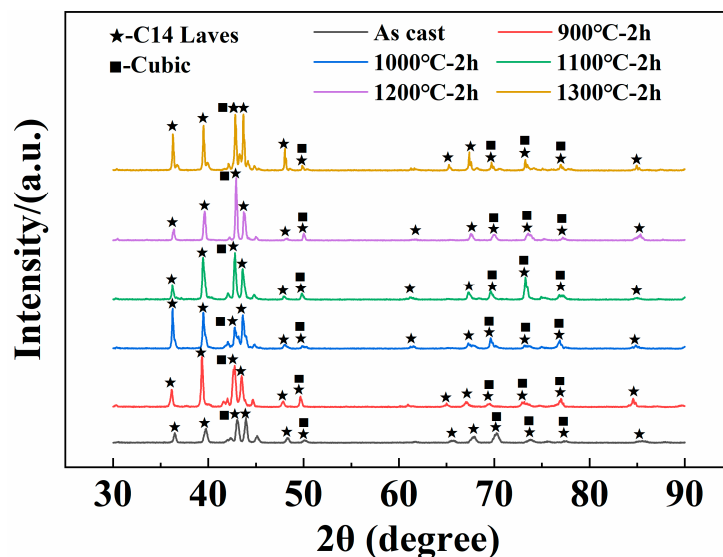


**Figure 1.** XRD patterns of the TiZrCrMnFeNi high-entropy alloy.

Moreover, as the heat-treatment temperature is increased, the diffraction peak angles of the C14 Laves phase exhibit shifts, as shown in Table 2. This phenomenon is particularly noteworthy as it suggests that lattice distortion has occurred within the alloy structure. The shifting of peak angles is often associated with changes in the unit cell volume, which can be attributed to the thermal expansion or contraction of the lattice parameters during the annealing process. Such alterations in the lattice structure can significantly impact the mechanical and physical properties of the high-entropy alloy, making it crucial to understand and control these changes through precise heat-treatment protocols.

**Table 2.** Main diffraction peak angles of TiZrCrMnFeNi high-entropy alloy under different heat-treatment annealing temperatures.

Sample	Main Diffraction Peak Angle ( $\theta$ )					
As-Cast	36.480	39.759	43.002	43.940	48.282	50.138
900 °C	36.160	39.323	42.761	43.500	47.841	49.660
1000 °C	36.258	39.479	42.779	43.620	48.079	49.841
1100 °C	36.223	39.441	42.799	43.600	47.979	49.821
1200 °C	36.397	39.620	42.920	43.721	48.291	50.020
1300 °C	36.283	39.499	42.821	43.679	48.036	49.861

To quantify the impact of annealing on the microstructure of the TiZrCrMnFeNi high-entropy alloy, the Rietveld method was employed to calculate the phase proportions and lattice parameters of the C14 Laves phase, with the results summarized in Table 3. The analysis reveals that the unit cell volume of the C14 Laves phase is strongly influenced by the annealing temperature. Notably, the content of the C14 Laves phase decreases significantly in alloys annealed at 900 °C and 1300 °C, while it increases for those annealed between 1000 °C and 1200 °C. These observations indicate that the annealing temperature plays a crucial role in stabilizing the C14 Laves phase, with an optimal range identified between 1000 °C and 1200 °C. This suggests that appropriate annealing conditions can effectively enhance the C14 Laves phase content, thereby potentially improving overall properties.

**Table 3.** XRD analysis results of TiZrCrMnFeNi HEA before hydrogen absorption.

Alloys	Phase	Lattice Parameter/ $\text{\AA}$ (C14 Laves Phase)	Unit Cell Volume/ $\text{\AA}^3$ (C14 Laves Phase)
As-Cast	C14 Laves (95.5%) + Cubic (4.5%)	$a = 4.93259; c = 8.03742$	169.36
900 °C	C14 Laves (81.3%) + Cubic (18.7%)	$a = 4.95507; c = 7.97617$	169.60
1000 °C	C14 Laves (96.3%) + Cubic (3.7%)	$a = 4.92544; c = 7.96313$	167.30
1100 °C	C14 Laves (96.9%) + Cubic (3.1%)	$a = 4.95462; c = 7.95379$	169.09
1200 °C	C14 Laves (98.9%) + Cubic (1.1%)	$a = 4.93250; c = 8.01737$	168.93
1300 °C	C14 Laves (83.7%) + Cubic (16.3%)	$a = 4.94705; c = 7.94097$	168.31

Microstructural analysis (Figure 2a–f) demonstrated that the alloy structure evolved from dendritic to equiaxed crystals as the annealing temperature increased, with precipitate phases predominantly distributed along grain boundaries. Related articles [16] have shown that within the TiZrCrMnFeNi HEA, Ti-rich and Ni-rich cubic phases precipitate both inside large grains and at grain boundaries, as illustrated in Figure 2g,h.

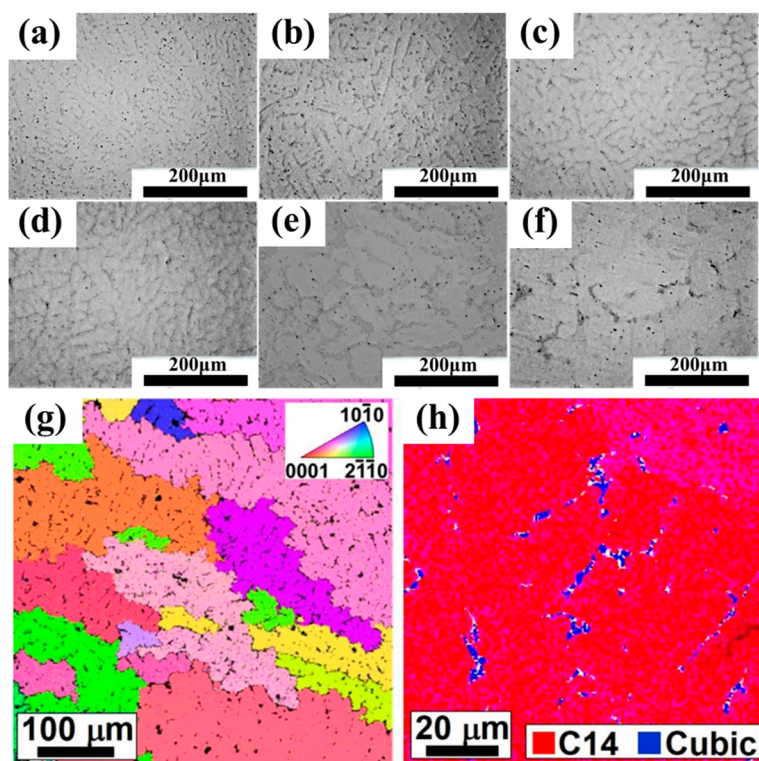


**Figure 2.** Microstructure of the TiZrCrMnFeNi high-entropy alloy (White color is mainly C14 Laves phase, and gray color is mainly cubic phase): (a) as-cast; (b) 900 °C; (c) 1000 °C; (d) 1100 °C; (e) 1200 °C; (f) 1300 °C; (g,h) EBSD analysis of the as-cast alloy [16]: C14 Laves phase (red color) and Cubic phase (blue color).

In the Figure 2g, the legend in the upper right corner shows the relationship between different colors and crystal orientations. These orientations are represented by Miller indices, which are used to describe specific crystal planes. The numbers “0001”, “10̄10” and “2̄110” represent three specific orientations of the crystal. Each color corresponds to a particular crystal orientation; for example, pink color may represent the “0001” orientation, blue color represents the “10̄10” orientation, and green color represents the “2̄110” orientation. Other colors in the figure indicate crystal orientations that lie between these three principal orientations, demonstrating the continuous variation of crystal orientation.

Meanwhile, Figure 2g shows that the material has large grains of C14 phase with grain sizes in the range of several hundred micrometers. In addition to these large grains, some fine microstructural features appear within these large grains as well as in the grain boundaries. Close examination of these fine microstructural features, as shown in Figure 2h, confirms that they correspond to the distribution of cubic phase within the C14 Laves phase.

Consequently, it can be inferred that the precipitate phases observed along the grain boundaries in the TiZrCrMnFeNi HEA are primarily cubic phases. Specifically, at 900 °C, cubic phase precipitates form extensively along the grain boundaries, indicating a high propensity for precipitation at this temperature. However, at 1300 °C, these precipitates undergo significant coarsening, which may be attributed to prolonged exposure to elevated temperatures that promote grain growth and coalescence of precipitates. In contrast, at intermediate annealing temperatures of 1000–1200 °C, cubic precipitates are more uniformly distributed and exhibit lower content, suggesting that these temperatures are optimal for achieving a fine and homogeneous precipitate distribution.

To evaluate the uniformity of elemental distribution within the alloy, EDS (energy-dispersive spectroscopy) spectral analysis was conducted on both as-cast and annealed microstructures, with the results presented in Figure 3. The analysis revealed that the

alloy annealed at 1200 °C exhibited the most uniform elemental distribution, significantly outperforming both the as-cast condition and the alloy annealed at 1300 °C. This finding indicates that annealing at 1200 °C promotes a more homogeneous distribution of elements throughout the alloy, likely due to the optimal thermal conditions that facilitate diffusion and mixing of the constituent elements. In contrast, improper annealing, such as at 1300 °C, can lead to excessive growth of cubic precipitates, which segregate certain elements and disrupt the overall microstructural uniformity. This highlights the importance of precise annealing temperature control in achieving desirable elemental homogeneity and maintaining the integrity of the alloy's microstructure.

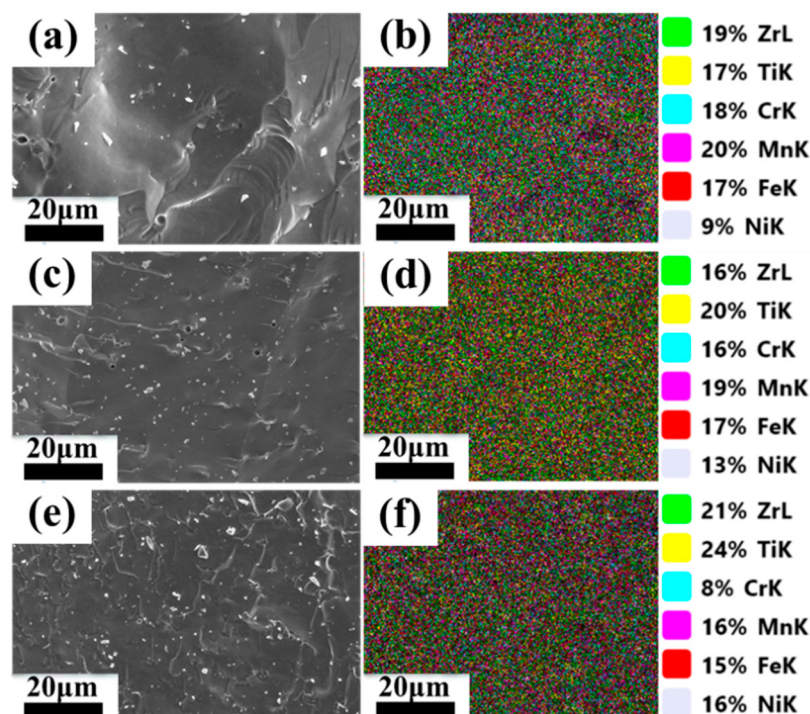


**Figure 3.** EDS analysis of the TiZrCrMnFeNi high-entropy alloy: (a,b) as-cast alloy; (c,d) alloy annealed at 1200 °C; (e,f) alloy annealed at 1300 °C.

### 3.2. Hydrogen Absorption KINETICS

To comprehensively evaluate the hydrogen storage performance of the TiZrCrMnFeNi high-entropy alloy, hydrogen absorption kinetics tests were conducted at 30 °C, as shown in Figure 4. The results in Figure 4a demonstrate that all alloy materials achieved their maximum hydrogen absorption capacity during the initial hydrogenation process without requiring any activation treatment. This indicates that the alloy inherently possesses excellent hydrogen absorption properties from the outset. However, Figure 4b reveals a significant decline in hydrogen absorption capacity when the annealing temperature was set at 900 °C and 1300 °C. As the annealing temperature increased to 1200 °C, the hydrogen absorption capacity of the alloy gradually recovered to 1.77 wt.%, although the rate of hydrogen absorption slowed considerably. This suggests that while the alloy's hydrogen storage capacity improves at this temperature, the kinetics of hydrogen absorption are hindered, likely due to changes in the microstructure that affect diffusion pathways and reaction kinetics.

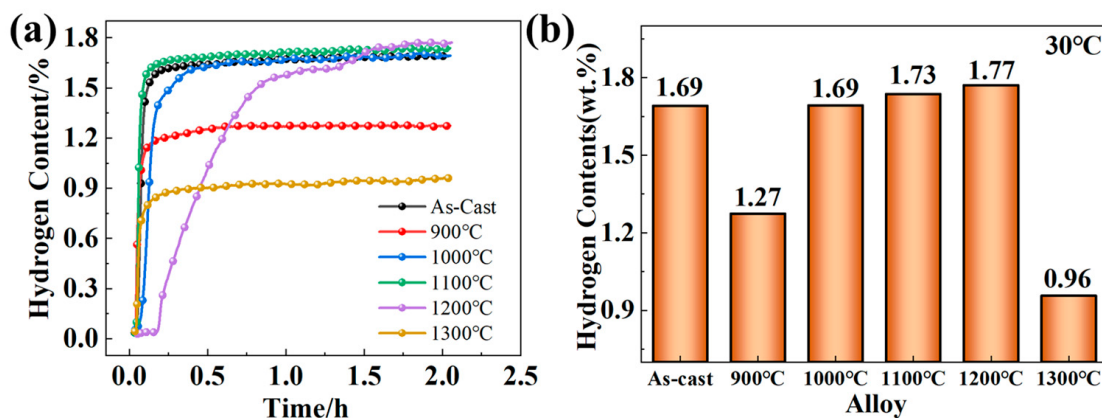


**Figure 4.** Analysis of hydrogen storage performance of the TiZrCrMnFeNi HEA: (a) initial hydrogen absorption kinetics curves for as-cast and annealed alloys; (b) hydrogen storage capacity for various alloy compositions.

Table 3 shows that the content of the C14 Laves phase in the alloy decreases significantly after annealing at both 900 °C and 1300 °C. The presence of the C14 phase has been reported to enhance hydrogen storage capacity by facilitating hydrogen diffusion [27–29]. The reduction in this phase content is critical. The content of the C14 Laves phase in the alloy decreased significantly after annealing at 900 °C and 1300 °C, which severely affected the hydrogen storage performance of the alloy. Additionally, EDS analysis presented in Figure 3 reveals that the elemental distribution becomes uneven following annealing at 1300 °C. This uneven distribution, combined with the significant reduction in the C14 Laves phase content, collectively contributes to the poor hydrogen absorption performance observed at these annealing temperatures. When the annealing temperature was raised to 1300 °C, there was another dramatic drop in hydrogen absorption capacity, further highlighting the detrimental effects of excessive heat treatment on the alloy's hydrogen storage capabilities. These findings underscore the importance of optimizing annealing conditions to balance the hydrogen absorption capacity and kinetics, thereby enhancing the overall performance of the alloy for hydrogen storage applications.

### 3.3. Curves and Effective Hydrogen Storage Capacity

To further elucidate the hydrogen storage performance of the alloy, a comprehensive hydrogen absorption/desorption pressure–composition–temperature (PCT) test was conducted across a temperature range of 0–60 °C. The plateau pressures for both hydrogen absorption and desorption were meticulously analyzed and statistically determined, with the results presented in Figures 5 and 6. The PCT curves reveal that all alloy materials are capable of achieving complete hydrogen desorption at 30 °C, indicating that the annealing heat treatment does not compromise the alloy's ability to reversibly absorb and desorb hydrogen. This finding is significant as it suggests that the alloy retains its full dehydrogenation capability regardless of the annealing conditions. However, it is noteworthy that the plateau pressures for hydrogen absorption and desorption exhibit substantial variations following annealing heat treatments at different temperatures. This implies that while the overall reversibility of hydrogen storage is maintained, the specific conditions of annealing significantly influence the thermodynamic and kinetic properties associated with hydrogen absorption and desorption, thereby affecting the alloy's performance in practical hydrogen storage applications.

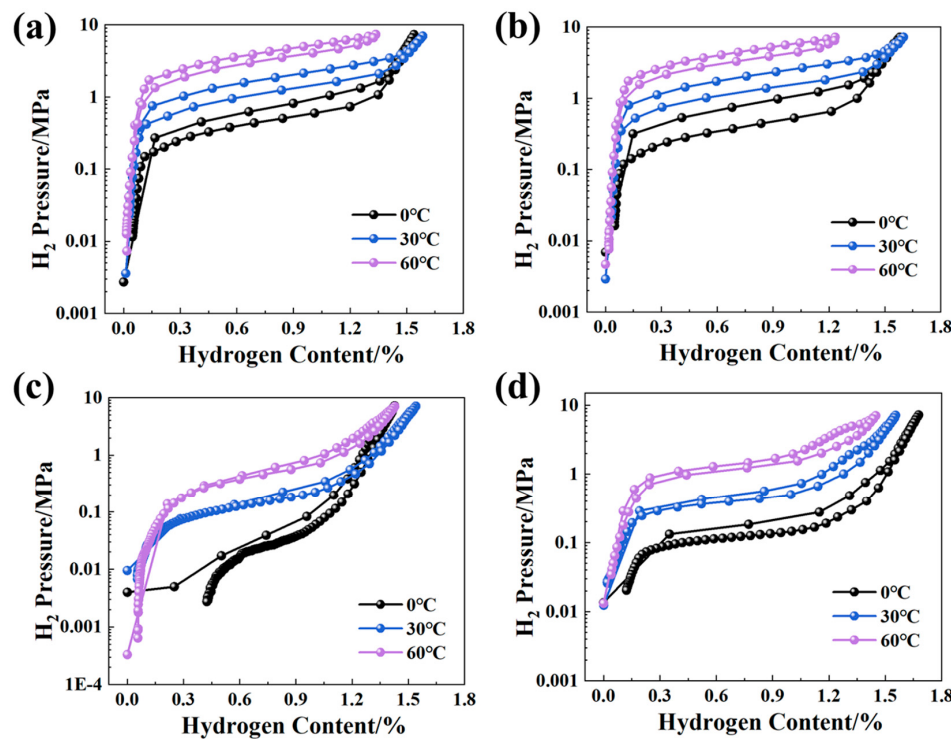


**Figure 5.** PCT curves for hydrogen absorption/desorption of the TiZrCrMnFeNi HEA at 0 °C (black color), 30 °C (blue color) and 60 °C (purple color): (a) as-cast alloy; (b) 1000 °C annealed alloy; (c) 1100 °C annealed alloy; (d) 1200 °C annealed alloy.

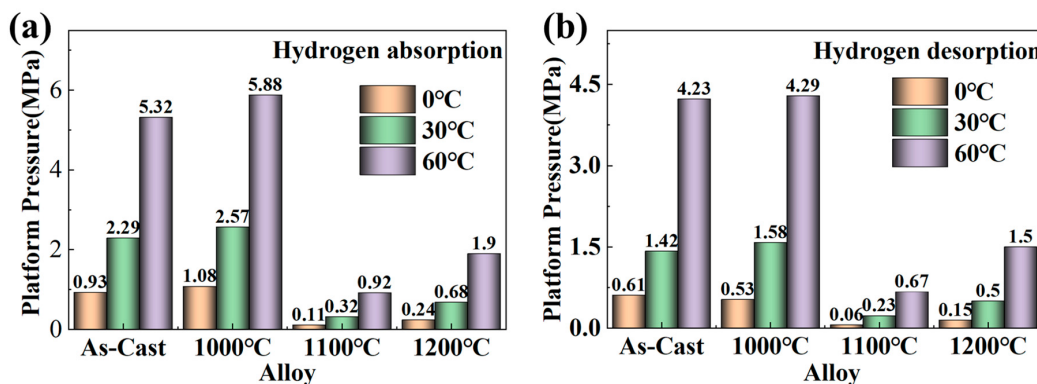


**Figure 6.** Hydrogen absorption/desorption plateau pressure of TiZrCrMnFeNi high-entropy alloy: (a) hydrogen absorption; (b) hydrogen desorption.

To explore the reasons for the changes in the plateau pressure of hydrogen absorption/desorption after annealing heat treatment, a trend diagram of the plateau pressure of hydrogen absorption and desorption versus the unit cell volume was plotted, as shown in Figure 7. It can be observed from the figure that an increase in the unit cell volume leads to a decrease in the plateau pressure. This is because a larger unit cell volume results in larger intermetallic voids within the alloy, which enhances hydrogen absorption and stabilizes the formed hydrides, thereby reducing the hydrogen desorption plateau pressure [30]. This also provides a rational explanation for the lowest hydrogen absorption and desorption plateau pressure observed at 1100 °C.

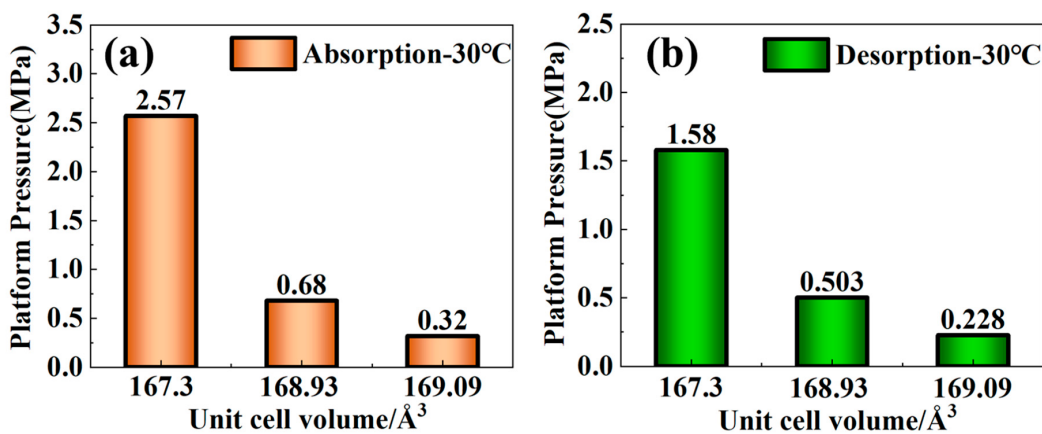


**Figure 7.** Plateau pressure versus unit cell volume of the TiZrCrMnFeNi high-entropy alloy: (a) curve of hydrogen absorption plateau pressure versus unit cell volume; (b) curve of hydrogen desorption plateau pressure versus unit cell volume.

### 3.4. Thermodynamic Characteristics

Based on the PCT curves and plateau pressure data presented in Figures 5 and 6, the enthalpy change ( $\Delta H$ ) and entropy change ( $\Delta S$ ) during the hydrogen absorption and desorption processes were calculated using the Van't Hoff equation. The results are shown in Figure 8. This approach allows for a detailed thermodynamic analysis of the hydrogen storage behavior of the alloy, revealing how the annealing treatments influence the energy required for hydrogen absorption and desorption. The calculated  $\Delta H$  and  $\Delta S$  values provide critical insights into the stability and kinetics of hydrogen storage, which are essential for optimizing the alloy's performance in practical applications. The Van't Hoff equation is shown in Equation (1):

$$\ln(P) = -\frac{\Delta H}{RT} + \frac{\Delta S}{R} \quad (1)$$

where  $P$  represents the equilibrium pressure during the hydrogen absorption/desorption processes (MPa),  $\Delta H$  denotes the enthalpy change (J/mol),  $\Delta S$  signifies the entropy change ( $\text{J}\cdot\text{mol}^{-1}\cdot\text{K}^{-1}$ ),  $T$  is the temperature (K), and  $R$  is the gas constant (8.314 J/(mol·K)).

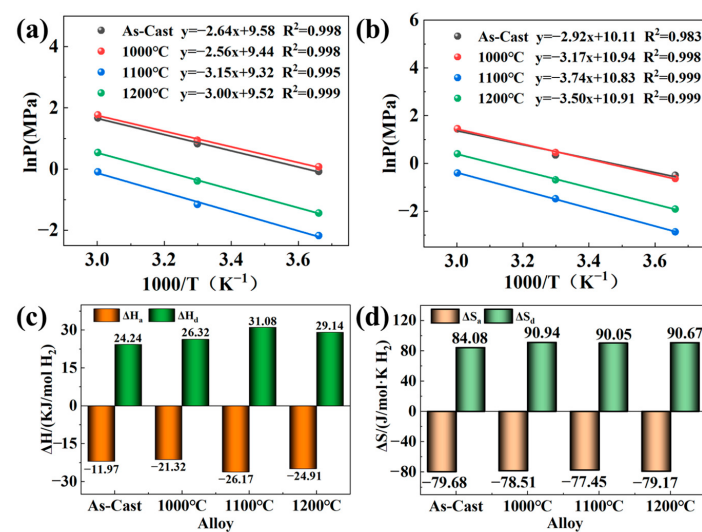


**Figure 8.** Calculation for enthalpy and entropy changes in the hydrogen absorption/desorption processes of the TiZrCrMnFeNi high-entropy alloy: (a) Van't Hoff plots for hydrogen absorption; (b) Van't Hoff plots for hydrogen desorption; (c) enthalpy and entropy changes for hydrogen absorption; (d) enthalpy and entropy changes for hydrogen desorption.

Figure 8a–d demonstrate that significant changes in the enthalpy and entropy during the hydrogen absorption and desorption processes occur after annealing treatments at various temperatures. These changes are closely related to the structural modifications induced by annealing, particularly in the C14 Laves phase of the alloy, where the unit cell volume is notably affected. To further investigate how these structural alterations influence hydrogen absorption and desorption, the relationship between the unit cell volume and the enthalpy change during these processes was analyzed. The resulting curves, shown in Figure 9, provide valuable insights into how the variations in unit cell volume impact the thermodynamics of hydrogen storage.

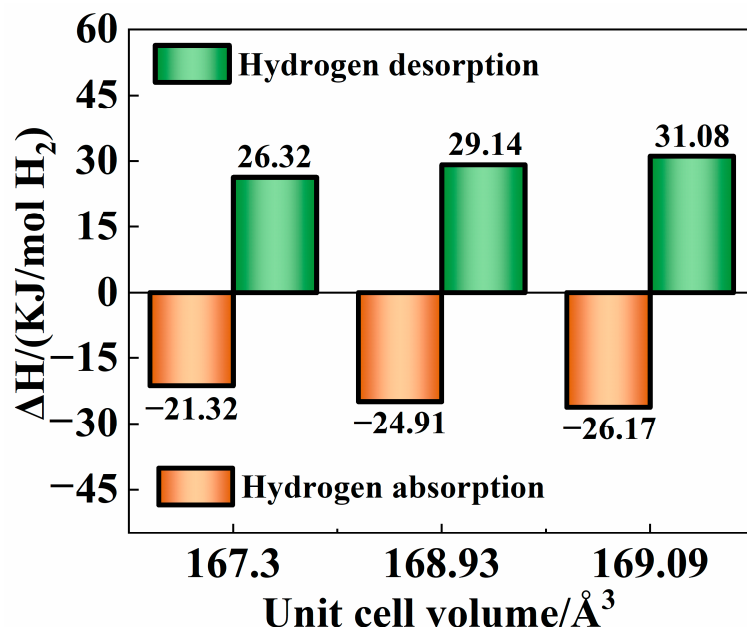


**Figure 9.** Diagram showing the enthalpy change in hydrogen absorption/desorption with unit cell volume.

Figure 9 illustrates that the unit cell volume of the C14 Laves phase is directly proportional to the absolute value of the enthalpy change during hydrogen absorption and desorption. Specifically, a larger unit cell volume in the C14 Laves phase corresponds to a higher hydrogen desorption enthalpy for the alloy. This relationship indicates that a greater amount of heat is required for dehydrogenation, thereby making the hydrogen desorption reaction more difficult. This finding reaffirms that an increase in cell volume leads to increased difficulty in hydrogen desorption. For instance, the alloy annealed at 1100 °C exhibits the largest unit cell volume for the C14 Laves phase, resulting in the formation of the most stable hydrides. These hydrides require more energy to decompose and release hydrogen, thus showing the highest enthalpy change for desorption and making the desorption reaction more challenging, as evidenced by the PCT curve at 0 °C in Figure 5c. Consequently, by optimizing heat-treatment processes, it is possible to enhance hydrogen storage density while also effectively controlling the thermal changes associated with hydrogen absorption and desorption reactions. This approach provides valuable guidance for the engineering application of high-entropy hydrogen storage alloy materials, enabling the development of more efficient and practical hydrogen storage solutions.

#### 4. Conclusions

Based on the alloy phase diagram, an annealing heat-treatment process ranging from 900 to 1300 °C was designed to systematically study the effects of different annealing temperatures on the hydrogen storage performance.

(1) After annealing heat treatment at various temperatures, all of the microstructure, elemental distribution, and hydrogen absorption/desorption performance of the TiZrCrMnFeNi high-entropy alloy changed. Inappropriate annealing treatments (at 900 °C and 1300 °C) led to a significant decrease in the content of the C14 Laves phase and non-uniform distribution of elements, which in turn caused a substantial reduction in hydrogen storage density. Conversely, appropriate annealing treatments (at 1000–1200 °C) promoted uniform distribution of elements and an increase in the content of the C14 Laves phase, thereby enhancing the hydrogen storage density of the alloy.

(2) When annealing at 1200 °C, the alloy achieves its maximum hydrogen absorption capacity (1.77 wt.%), and alloys annealed between 1000 and 1200 °C can be completely dehydrogenated at 30 °C. Annealing heat treatment does not affect the reversibility of hydrogen absorption\desorption in TiZrCrMnFeNi high-entropy alloy. This characteristic is very important for practical applications. In practical applications, alloys often need to undergo multiple hydrogen absorption/desorption.

(3) The unit cell volume of the C14 Laves phase in the alloy changes after annealing heat treatment. An increase in the unit cell volume results in a lower dehydrogenation plateau pressure, which is attributed to the enlarged interstitial spaces within the lattice. These expanded spaces facilitate hydrogen atom occupation, thereby enhancing the stability of the hydrides. Consequently, the enthalpy change in dehydrogenation increases, and the desorption reaction becomes more difficult to proceed.

**Author Contributions:** Writing—original draft, writing—review and editing, supervision, funding acquisition, T.C.; writing—review and editing, investigation, formal analysis, data curation, J.H.; writing—original draft, supervision, investigation, methodology, W.F.; methodology, funding acquisition, conceptualization, L.H.; validation, X.D.; investigation, methodology, G.Z.; validation, funding acquisition, X.L.; methodology, X.R. All authors have read and agreed to the published version of the manuscript.

**Funding:** This research is financially supported by the Major Science and Technology Project of China National Machinery Industry Corporation (X.L. ZDZX2024-10), the Anhui Province Major Industrial Innovation Program (X.L. AHZDCYCX-LSDT2023-07), the Youth Science and Technology Fund Project of China Machinery Industry Group Co., Ltd. (L.H. QNJJ-ZD-2022-01), the Youth Science and Technology Project of China National Machinery Industry Corporation (X.L. QNJJ-PY-2023-02), the Youth Science and Technology Foundation of Hefei General Machinery Research Institute (T.C. 2023010787), and the Major Science and Technology Project of China National Machinery Industry Corporation (X.L. SINOMAST-ZDZX-2018-01).

**Data Availability Statement:** Data will be made available on request.

**Conflicts of Interest:** Author Tengfei Cheng, Jing Huang, Wanggang Fang, Liqing He, Xiangqun Duan, Xiao Li and Xinghai Ren were employed by the company Hefei General Machinery Research Institute Co., Ltd. The remaining authors declare that the research was conducted in the absence of any commercial or financial relationships that could be construed as a potential conflict of interest.

## References

1. Yu, X.; Tang, Z.; Sun, D.; Ouyang, L.; Zhu, M. Recent advances and remaining challenges of nanostructured materials for hydrogen storage applications. *Prog. Mater. Sci.* **2017**, *88*, 1–48. [[CrossRef](#)]
2. Bashir, M.F.; Pata, U.K.; Shahzad, L. Linking climate change, energy transition and renewable energy investments to combat energy security risks: Evidence from top energy consuming economies. *Energy* **2025**, *314*, 134175. [[CrossRef](#)]
3. Lee, H.; Ahn, J.; Choi, D.G.; Park, S.Y. Analysis of the role of hydrogen energy in achieving carbon neutrality by 2050: A case study of the Republic of Korea. *Energy* **2024**, *304*, 132023. [[CrossRef](#)]
4. Bhuiyan, M.M.H.; Siddique, Z. Hydrogen as an alternative fuel: A comprehensive review of challenges and opportunities in production, storage, and transportation. *Int. J. Hydrogen Energy* **2025**, *102*, 1026–1044. [[CrossRef](#)]

5. Wang, Z.; Huang, C.; Zhang, Y.; Zhong, F.; Li, W. Tackling carbon peak and carbon neutrality challenges: A method with long-range energy alternatives planning system and Logarithmic Mean Divisia Index Integration. *Energy* **2024**, *311*, 133465. [[CrossRef](#)]
6. He, T.; Pachfule, P.; Wu, H.; Xu, Q.; Chen, P. Hydrogen carriers. *Nat. Rev. Mater.* **2016**, *1*, 16059. [[CrossRef](#)]
7. Hui, Y.; Wang, M.; Guo, S.; Akhtar, S.; Bhattacharya, S.; Dai, B.; Yu, J. Comprehensive review of development and applications of hydrogen energy technologies in China for carbon neutrality: Technology advances and challenges. *Energy Convers. Manag.* **2024**, *315*, 118776. [[CrossRef](#)]
8. Terlouw, T.; Rosa, L.; Bauer, C.; McKenna, R. Future hydrogen economies imply environmental trade-offs and a supply-demand mismatch. *Nat. Commun.* **2024**, *15*, 7043. [[CrossRef](#)]
9. Yeh, J.W.; Chen, S.K.; Lin, S.J.; Gan, J.Y.; Chin, T.S.; Shun, T.T.; Tsau, C.H.; Chang, S.Y. Nanostructured High-Entropy Alloys with Multiple Principal Elements: Novel Alloy Design Concepts and Outcomes. *Adv. Eng. Mater.* **2004**, *6*, 299–303. [[CrossRef](#)]
10. Cantor, B.; Chang, I.T.H.; Knight, P.; Vincent, A.J.B. Microstructural development in equiatomic multicomponent alloys. *Mater. Sci. Eng. A* **2004**, *375*, 375–377. [[CrossRef](#)]
11. Miracle, D.B.; Senkov, O.N. A critical review of high entropy alloys and related concepts. *Acta Mater.* **2017**, *122*, 448–511. [[CrossRef](#)]
12. Senkov, O.N.; Miracle, D.B.; Chaput, K.J.; Couzinie, J.P. Development and exploration of refractory high entropy alloys—a review. *J. Mater. Res.* **2018**, *33*, 3092–3128. [[CrossRef](#)]
13. Li, S.; Hu, H.; Zhang, X.; Li, C.; Liu, Y.; Liu, L.; Chen, Q. Hydrogen storage in a novel BCC-structured TiCrW alloys. *Chem. Eng. J.* **2025**, *503*, 157872. [[CrossRef](#)]
14. Elman, R.; Kudiarov, V.; Sayadyan, A.; Pushilina, N.; Leng, H. Performance improvement of magnesium-based hydrogen storage tanks by using carbon nanotubes addition and finned heat exchanger: Numerical simulation and experimental verification. *Int. J. Hydrogen Energy* **2024**, *92*, 1375–1388. [[CrossRef](#)]
15. Qureshi, T.; Khan, M.M.; Pali, H.S. The future of hydrogen economy: Role of high entropy alloys in hydrogen storage. *J. Alloys Compd.* **2024**, *1004*, 175668. [[CrossRef](#)]
16. Edalati, P.; Floriano, R.; Mohammadi, A.; Li, Y.T.; Zepon, G.; Li, H.W.; Edalati, K. Reversible room temperature hydrogen storage in high-entropy alloy TiZrCrMnFeNi. *Scr. Mater.* **2020**, *178*, 387–390. [[CrossRef](#)]
17. Chen, X.Y.; Liu, B.; Zhang, S.B.; Ding, X.; Chen, R.R. Effect of heat treatment on microstructure and thermal stability of Ti19Hf4V40Mn35Cr2 hydrogen storage alloy. *J. Alloy. Compd.* **2022**, *917*, 165355. [[CrossRef](#)]
18. Zhou, H.Y.; Wang, F.; Wang, J.; Wang, Z.M.; Yao, Q.R.; Deng, J.Q.; Tang, C.Y.; Rao, G.H. Hydrogen storage properties and thermal stability of V35Ti20Cr45 alloy by heat treatment. *Int. J. Hydrogen Energy* **2014**, *39*, 14887–14895. [[CrossRef](#)]
19. Ma, P.; Wu, E.D.; Li, W.H.; Sun, K.; Chen, D.F. Microstructures and hydrogen storage properties of  $Ti_{0.7}Zr_{0.3}(Cr_{1-x}V_x)_2$  Alloys. *Acta Metall. Sin.* **2014**, *50*, 454–462. Available online: <https://www.ams.org.cn/CN/10.3724/SPJ.1037.2013.00637> (accessed on 3 December 2024).
20. Sato, T.; Saitoh, H.; Utsumi, R.; Ito, J.; Nakahira, Y.; Obama, K.; Takagi, S.; Orimo, S.-I. Hydrogen Absorption Reactions of Hydrogen Storage Alloy LaNi<sub>5</sub> under High Pressure. *Molecules* **2023**, *28*, 1256. [[CrossRef](#)]
21. Liu, Y.; Chabane, D.; Elkadem, O. Optimization of LaNi<sub>5</sub> hydrogen storage properties by the combination of mechanical alloying and element substitution. *Int. J. Hydrogen Energy* **2024**, *53*, 394–402. [[CrossRef](#)]
22. Xu, R.; Cheng, T.; Li, C.; Yang, X.; Rong, J. Properties of Ti-Based Hydrogen Storage Alloy. *J. Power Energy Eng.* **2024**, *12*, 99–114. [[CrossRef](#)]
23. Jiao, H.; Wu, Y.; Guo, X.; Wang, S.; Jiang, L.; Wang, S.; Hao, L.; Tan, G. Optimization of V-Ti-Fe hydrogen storage alloy based on orthogonal experiments. *J. Alloys Compd.* **2024**, *1002*, 175262. [[CrossRef](#)]
24. Wang, M.; Wang, Y.; Kong, H.; Xie, Q.; Wu, C.; Wang, Y.; Chen, Y.; Yan, Y. Development of Fe-containing BCC hydrogen storage alloys with high vanadium concentration. *J. Alloys Compd.* **2023**, *958*, 170294. [[CrossRef](#)]
25. Vajo, J.J.; Mertens, F.; Ahn, C.C.; Bowman, R.C.; Fultz, B. Altering Hydrogen Storage Properties by Hydride Destabilization through Alloy Formation: LiH and MgH<sub>2</sub> Destabilized with Si. *J. Phys. Chem. B* **2004**, *108*, 13977–13983. [[CrossRef](#)]
26. Chen, X.; Zou, J.; Zeng, X.; Ding, W. Hydrogen storage in Mg<sub>2</sub>Fe(Ni)H<sub>6</sub> nanowires synthesized from coarse-grained Mg and nano sized γ-Fe(Ni) precursors. *Int. J. Hydrogen Energy* **2016**, *41*, 14795–14806. [[CrossRef](#)]
27. Liang, J.; Li, G.; Ding, X.; Wen, Z.; Zhang, T.; Qu, Y. The synergistic effect of Ni and C14 Laves phase on the hydrogen storage properties of TiVZrNbNi high entropy hydrogen storage alloy. *Intermetallics* **2024**, *164*, 108102. [[CrossRef](#)]
28. Liang, J.; Li, G.; Ding, X.; Wen, Z.; Zhang, T.; Qu, Y. Effect of C14 Laves/BCC on microstructure and hydrogen storage properties of (Ti<sub>32.5</sub>V<sub>27.5</sub>Zr<sub>7.5</sub>Nb<sub>32.5</sub>)<sub>1-x</sub>Fe<sub>x</sub> (x = 0.03, 0.06, 0.09) high entropy hydrogen storage alloys. *J. Energy Storage* **2023**, *73*, 108852. [[CrossRef](#)]

29. Li, G.; Li, Y.; Liang, J.; Wen, Z.; Zhang, T.; Ding, X.; Qu, Y. Influence of C14 Laves phase and Zr-rich phase interactions on the hydrogen storage properties of  $Ti_{32.5}V_{27.5}Zr_{7.5}Nb_{32.5}$  high entropy hydrogen storage alloy. *Intermetallics* **2024**, *168*, 108239. [[CrossRef](#)]
30. Zhu, Y.Y.; Yang, X.S.; Xu, Z.L.; Tsui, G.C.; Zhou, Q.; Tang, R.H.; Xiao, F.M.; Chan, K.C. Development of AB2-type  $TiZrCrMnFeCoV$  intermetallic high-entropy alloy for reversible room-temperature hydrogen storage. *J. Energy Storage* **2024**, *75*, 109553. [[CrossRef](#)]

**Disclaimer/Publisher’s Note:** The statements, opinions and data contained in all publications are solely those of the individual author(s) and contributor(s) and not of MDPI and/or the editor(s). MDPI and/or the editor(s) disclaim responsibility for any injury to people or property resulting from any ideas, methods, instructions or products referred to in the content.